Ferrimagnetic spin waves in honeycomb and triangular layers of math xmlns="http://www.w3.org/1998/Math/MathML">msub>mi mathvariant="normal">Mn/mi>mn>3/mn>/msub>msub> mi mathvariant="normal">Si/mi>mn>2/mn> /msub>msub>mi mathvariant="normal">Te/mi> mn>6/mn>/msub>/math>

G. Sala, J. Y. Y. Lin, A. M. Samarakoon, D. S. Parker, A. F. May, and M. B. Stone

Phys. Rev. B **105**, 214405 — Published 6 June 2022

DOI: 10.1103/PhysRevB.105.214405

Ferrimagnetic spin-waves in the honeycomb and triangular layers of $Mn_3Si_2Te_6$*

G. Sala,[1] J. Y. Y. Lin,[1] A. M. Samarakoon,[2,3] D. S. Parker,[4] A. F. May,[4] and M. B. Stone[2,†]

[1]*Spallation Neutron Source, Second Target Station, Oak Ridge National Laboratory, Oak Ridge, Tennessee 37831, USA*

[2]*Neutron Scattering Division, Oak Ridge National Laboratory, Oak Ridge, Tennessee 37831, USA*

[3]*Materials Science Division, Argonne National Laboratory, Lemont, Illinois 60439, USA*

[4]*Materials Science and Technology Division, Oak Ridge National Laboratory, Oak Ridge, Tennessee 37831, USA*

(Dated: May 19, 2022)

A detailed analysis of the ferrimagnetic ground state of $Mn_3Si_2Te_6$ has been performed using inelastic neutron scattering. Although the proposed valence of the nominal Mn^{2+} ions would have quenched orbital angular momentum, a significant exchange anisotropy exists in $Mn_3Si_2Te_6$. This apparent exchange anisotropy is a manifestation of a weak spin-orbit coupling in the layered material. We employ a detailed simulation of the spin-wave spectrum coupling traditional refinement of dispersion parameters to image analysis techniques, while including Monte Carlo simulations of the instrumental resolution to accurately identify the exchange couplings to the third nearest neighbor. An independent validation of our results is made by comparing our final Hamiltonian to heat capacity measurements.

PACS numbers: 75.10.Jm, 78.70.Nx, 75.50.Gg

I. INTRODUCTION

Research has accelerated examining quantum materials with quasi-two-dimensional magnetic interactions. Physical examples of such systems are generally crystallographically layered with significant exchange interactions within planes and weaker interplane exchange interactions. Van der Waals compounds, i.e. compounds held together by Van der Waals bonds, with exchange interactions[1–3] are one sub-class of these materials. Other materials in this diverse family include cuprate[4] and iron-based superconductors[5], quasi-two-dimensional Mott insulators[6,7], as well as inter-metallic materials[8,9]. This has been largely driven by the now-realized prospect of building heterostructures from materials with complementary properties.[10–12] Within this context two-dimensional (2D) and quasi-2D materials are of fundamental interest from a bulk perspective, because they often manifest strong in-plane interactions and weak inter-plane interactions. For instance, the compounds $FePS_3$, $CrSiTe_3$, $MnPS_3$, and CrI_3 have layers connected by van der Waals bonds, and demonstrate bulk magnetic ordering with anisotropic interactions yielding anisotropic properties, suppressed 3D ordering temperatures, two-dimensional order, and persistent short-range correlations above T_C.[13–16]

We have chosen to examine the layered, three-dimensional ferrimagnetic system $Mn_3Si_2Te_6$ to look for predicted anisotropic exchange terms in the spin Hamiltonian. The layered structure is similar to recently examined magnetic van der Waals compounds albeit in a 3D material. Understanding the nature of the anisotropic interactions and spin-orbit coupling in $Mn_3Si_2Te_6$ has implications for both frustrated 3D materials as well as 2D van der Waals compounds. $Mn_3Si_2Te_6$ was first described as a semiconducting ferrimagnetic material with the stoichiometry $MnSiTe_3$[18]. This early work characterized the ordering temperature as $T_c = 82$ K, an antiferromagnetic Curie-Weiss temperature of $\Theta_{CW} = 75$ K, and a significant anisotropic magnetization between the a and c axes. The stoichiometry was later corrected and the crystal structure was refined to be trigonal (space group $P\bar{3}1c$, No. 163) with room temperature lattice constants $a = 7.029(2)$ and $c = 14.255(3)$ Å[17]. Importantly, the crystal structure was shown to be three-dimensional, with Mn atoms filling octahedral voids so that there is not a Van der Waals gap in $Mn_3Si_2Te_6$. Figure 1 illustrates the crystal structure. The lattice consists of planes of Mn^{2+} ions ($S = 5/2$, $L = 0$) alternating with planes of Te and Si atoms along the c-axis as shown in Fig. 1(a)[17,18]. The Mn^{2+} sites are arranged in two types of layers which alternate along the c-axis. One layer of Mn atoms (Mn1) has a honeycomb structure, shown as red spheres in Fig. 1, and the other layer of Mn atoms (Mn2) are arranged in a sparser triangular lattice, blue spheres in Fig. 1. Note that the Mn2 sites are not immediately aligned with the Mn2 sites in the neighboring layers. This results in the genesis of an ABACAB stacking pattern in the crystal structure[17].

Recently, a long range magnetic ordered phase was characterized below $T_c \approx 78$ K. This phase consists of ferromagnetically aligned moments in the ab-plane with

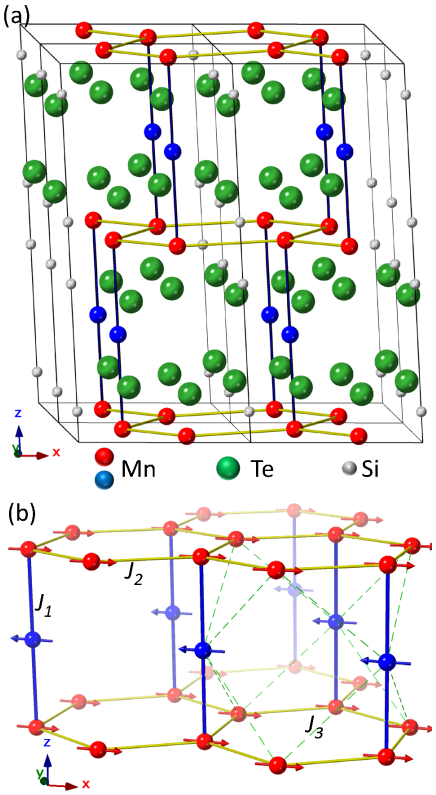

FIG. 1: (a) Crystal structure of the $Mn_3Si_2Te_6$ trigonal unit cell showing the layered arrangement of the Mn^{2+} ions and the location of the Te and Si sites[17]. The two non equivalent Mn sites are illustrated with red (Mn1 on the $4f$ site) and blue (Mn2 on the $2c$ site) spheres. (b) Ordered magnetic structure of $Mn_3Si_2Te_6$ and proposed exchange couplings between magnetic sites. The arrows represent the easy-plane direction of the spins in the ordered phase. The exchange J_1 is shown as a blue line between Mn sites. The exchange J_2 is shown as a yellow line within the honeycomb layers of the Mn sites. The exchange J_3, dashed green lines, is only shown for one portion of the lattice for clarity of the figure.

an anti-ferromagnetic alignment of moments for neighboring spins along the c-axis[19]. The difference in the number of Mn sites in the two layers leads to an overall bulk ferrimagnetic behavior of the system. First-principles calculations established a likely competition between anti-ferromagnetic exchange interactions up to the third nearest neighbor Mn-Mn bonds. These geometrically frustrated interactions are illustrated as J_1, J_2, and J_3 in Fig. 1(b), and the ferrimagnetic ground state results from a dominance of the longer-range J_3 over J_2. Density Functional Theory (DFT) calculations also proposed a finite amount of spin-orbit coupling to exist in the Hamiltonian, calling into question the nominal Mn^{2+} with a quenched orbital moment[19], the magnetism displays a large anisotropy on the order of 10 Tesla at $T = 5$ K further suggesting the existence of this spin-orbit term in the relevant interactions in the magnetic Hamiltonian.

In the current study, we use inelastic neutron scattering to directly probe the spin-wave dispersion of $Mn_3Si_2Te_6$. We find that a Hamiltonian with anisotropic anti-ferromagnetic exchange is required to fully describe the resulting spectrum further validating the proposed spin-orbit interaction. The best model describes the dispersion, the heat capacity and the magnetic density of states accurately, and it also confirms the ground state spin orientation proposed in Ref.[19].

II. EXPERIMENTAL TECHNIQUES

$Mn_3Si_2Te_6$ was grown by chemical vapor transport (CVT) starting from the elements using iodine as a transport agent. The high-purity elements were sealed in a SiO_2 ampoule (Te Alfa Aesar 6N shot, Si Alfa Aesar 6N lump, Mn Alfa Aesar 99.98% granules). The ampoule was heated in a clam-shell furnace with a hot side kept at 800° C for 500h. The starting materials were kept on the hot side and crystals grew throughout the entire ampoule; a gradient of approximately 40 degrees over 15 cm existed. Sample orientation was first checked with x-ray diffraction off the as-grown facets and this verified a [001] normal orientation as expected. Magnetization measurements were utilized to further characterize the crystals and verify consistency with the previously reported melt-grown materials. The Curie temperature and anisotropy was observed to be consistent, however the CVT grown crystals do not contain an anomaly near 300 K that has been observed in melt-grown crystals and is speculated to result from some type of intrinsic defect. This difference between CVT and melt-grown $Mn_3Si_2Te_6$ has been discussed in Ref.[19,20].

A single crystal sample was wrapped in aluminum foil and wired to a thin aluminum plate. Inelastic neutron scattering measurements were performed at the Spallation Neutron Source at the Oak Ridge National Laboratory using this crystal with the $(H0L)$ plane in the scattering plane of the instruments. Measurements at the SEQUOIA spectrometer were performed with $E_i = 60$ meV incident energy neutrons with the sample mounted to the cold-finger of a bottom loading closed cycle refrigerator[21]. Measurements at the CNCS spectrometer were performed with $E_i = 12$ meV and the sample mounted to the sample stick of a liquid helium top-loading cryostat[22]. Both measurements were performed in high flux configurations of the instrument while rotating the sample about its vertical axis by at least 180 degrees with a spacing of 1 degrees to collect wave-vector dependent spectra throughout a volume of reciprocal space. The SEQUOIA/CNCS measurement was collected for 0.42/0.25 Coulombs of charge (≈ 5 min. / ≈ 3 min.) on the spallation target for each value of rotation angle. Measurements were performed at two different instruments to obtain reasonable energy resolution across the entire band of magnetic excitations. Measurements were performed at $T = 5$ K and $T = 100$ K. Finally, the entire four dimen-

sional set of data was reduced, normalised and properly symmetrized about the origin of the primary axes of the reciprocal lattice using the MANTID software package[23].

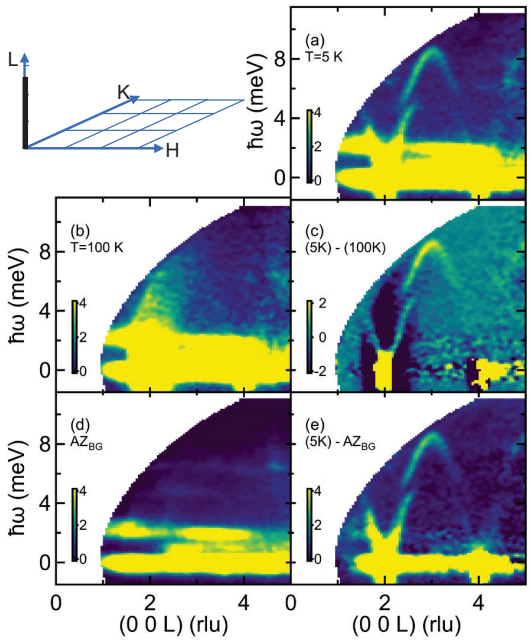

FIG. 2: Inelastic neutron scattering measurements of $Mn_3Si_2Te_6$ and background subtraction of this data. Each spectrum is shown on the same relative intensity with a color scale four units large. (a) $T = 5$ K measurement of the INS spectra for $Mn_3Si_2Te_6$ measured along the L-axis from the CNCS measurement. Data orthogonal to the wave-vector shown were integrated over a range of ± 0.1 reciprocal lattice units (rlu)(b) $T = 100$ K measurement of the INS spectra for $Mn_3Si_2Te_6$ measured along the L-axis from the CNCS measurement. (c) Difference of the data shown in panels (a) and (b) with the high temperature measurement subtracted from the low-temperature measurement. (d) Azimuthal determined background, AZ_{BG}, projected along the same direction as the data. (e) The difference between the $T = 5$ K measurement in panel (a) and the AZ_{BG} shown in panel (d). Inset in the upper left illustrates the path of the data through reciprocal space as a heavy black line.

A. Background Subtraction

The small sample size ($\approx$ 90 micro-moles of Mn, i.e. $\approx$ 49 mg) used in these measurements resulted in a relatively large background contribution from the scattering due to the sample mounting hardware, and the sample environment itself. In order to analyze the spin wave dispersion in detail for such a small sample, the background needs to be adequately quantified. The first approximation of using the high temperature, $T = 100$ K, measurement as a background for the low temperature, $T = 5$ K measurement was found to be problematic. Typically, above the ordering temperature, a band of magnetic scattering will often soften to lower energy transfers and weaken in intensity. Concomitantly, the higher temperature measurement will enhance the scattering intensity of phonons which may overlap or pass through the magnetic spectrum. Thus we found that both of these effects combined to produce a significantly over-subtracted low-temperature measurement when using the high temperature data as a background. Figure 2(a) and (b) illustrates the $T = 5$ K and $T = 100$ K scattering intensity as a function of energy transfer, $\hbar\omega$, for wave-vectors along the L-axis in reciprocal lattice units (rlu). At $T = 5$ K, a dispersive magnetic mode can be seen emerging from the (002) wave-vector. However, there is also significant scattering from the cryostat and/or sample mount for energies from 0 meV up to approximately 4 meV. The higher temperature measurement, (b) at $T = 100$ K, shows a broadening and softening of the magnetic mode to lower energy transfers and smaller values of wave-vector transfer. The difference of these two measurements, shown in Fig. 2 (c), is significantly over-subtracted near the $L = 2$ value. To avoid this, we use a heuristic approach similar to what has been done in Ref.[24] to quantify the background. For each incident energy, sample temperature measured and angular range, we generated a background data set based upon the detected neutrons within azimuthal sectors on the instrument detector which contributed to the lowest intensity for a given detector location and a small range of energy transfer.[25] The minimum scattering intensity for these sectors was chosen based upon the full range of rotation angles measured in each measurement. This azimuthally gleaned background, AZ_{BG}, is then traced back to its original neutron events and used to generate a separate file for background subtraction. This background is projected in reciprocal space in an identical manner as the original data, as shown in Fig. 2(d). The algorithm is able to quantify the significant background due to the powder scattering from the sample environment and sample mounting that is independent of the single crystal sample orientation. Figure 2(e), is the difference in the $T = 5$ K measurement and the AZ_{BG}. In this case there is no significant over-subtraction, and the second minimum in the dispersion can now be seen at $L = 4$. Unless otherwise stated, we apply this type of gleaned background subtraction to our presented measurements.

III. EXPERIMENTAL RESULTS AND DISCUSSION

Figure 3(a)-(d) shows the measured scattering intensity as a function of energy transfer, $\hbar\omega$, and wave-vector transfer along four particular directions within the reciprocal space of the crystal structure. Figure 4(a) shows the measured scattering intensity along the (H01) direction. We plot the lower energy transfer contours of the CNCS measurement on top of the SEQUOIA measurement to preserve reasonable energy resolution in different

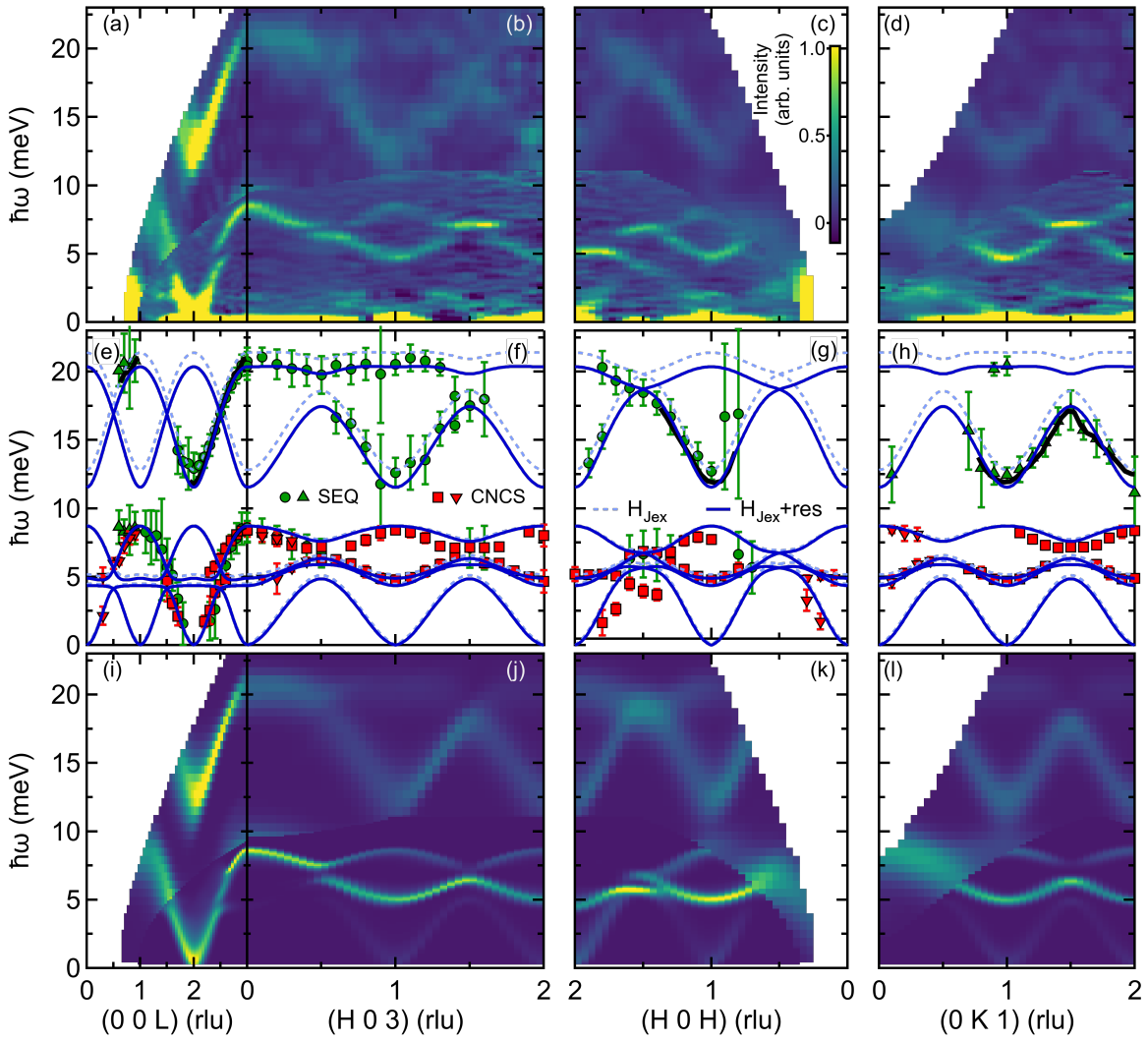

FIG. 3: Measured scattering intensity, determined spin-wave mode locations, calculated spin-wave dispersion and calculated scattering intensity for $Mn_3Si_2Te_6$ at T=5 K. (a)-(d) $T = 5$ K measured INS intensity. The slices in reciprocal space shown to higher/lower energy transfer are from the SEQUOIA/CNCS measurement. Data have been background subtracted as described in the text. The scattering intensity from SEQUOIA has been multiplied by a factor of 20 to place it on the same intensity scale as the CNCS data. (e)-(h) Determined spin-wave mode energies as a function of energy transfer and wave-vector transfer. Green/red points are from SEQUOIA/CNCS. Triangular symbols have energy values determined from higher Brillouin zones, but are shown at reduced wave-vector to appear in the figure. Mode values were determined from Gaussian fits to constant wave-vector scans as described in the text and illustrated in Fig. 5. Error bars are the half width at half maximum (HWHM) of the determined Gaussian peak added in quadrature to the fitted error in peak location. Dashed blue lines are the calculated spin-wave mode energies based upon the exchange parameters listed in Table I for the H_{Jex} model using spinW fits of only the dispersion. Heavy black lines correspond to resolution corrected dispersion based upon the image analysis described in the text. Solid blue lines are the calculated spin-wave mode energies based upon the exchange parameters listed in Table I for the H_{Jex} model using resolution corrected mode energies. (i)-(l) Calculated scattering intensity from convolution of MCViNE-calculated resolution function for both the SEQUOIA and CNCS measurements based upon the model with the exchange parameters determined from the resolution corrected dispersion analysis, $H_{Jex}^{\text{res.}}$, described in the text with the values listed in Table I. Data in panels (a)-(d) and (i)-(l) have been smoothed by a Gaussian smoothing algorithm.

portions of the excitation spectrum. The measurements show two ranges of scattering intensity populated with excitations. There is a higher energy band of excitations between approximately 12 and 22 meV, and there is a lower band of gapless excitations between 0 and 8 meV. In each of these regions there are at least two excitations that appear to cross one another. There is significant dispersion in the $(00L)$ direction and within the $(HK0)$ plane. However, there are also regions of reciprocal space that have flatter bands. The gap between

the lower and higher energy modes indicates that there is likely an anisotropic exchange term in the Hamiltonian. Significant single ion anisotropy is unlikely, given the lack of any gap in the spin-wave spectrum near zero energy transfer.

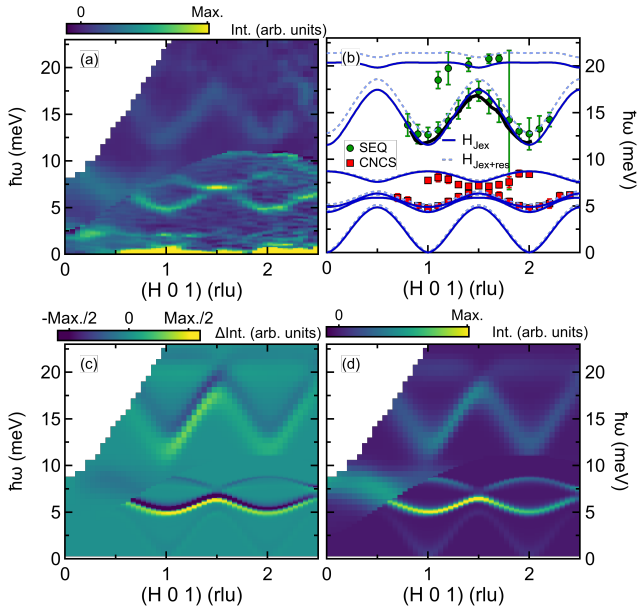

FIG. 4: (a) $T = 5$ K measured INS intensity along (H01). Slice which extends to higher/lower energy transfer is from the SEQUOIA/CNCS measurement. Data have been background subtracted as described in the text. The scattering intensity from SEQUOIA has been multiplied by a factor of 10 to place it on the same intensity scale as the CNCS data. (b) Determined spin-wave mode energies as a function of energy and wave-vector transfer. Green/red points are from the SEQUOIA/CNCS measurement. Mode values were determined from Gaussian fits to constant wave-vector scans as described in text and illustrated in Fig. 5. Error bars are the half width at half maximum (HWHM) of the determined Gaussian peak added in quadrature to the fitted error in peak location. Dashed blue lines are the calculated spin-wave mode energies based upon the exchange parameters listed in Table I for the H_{Jex} model using spinW fits of only the dispersion. Heavy black lines correspond to resolution corrected dispersion based upon the image analysis described in the text. Solid blue lines are the calculated spin-wave mode energies based upon the exchange parameters listed in Table I for the H_{Jex} model using resolution corrected mode energies. (c) Difference in calculated spin-wave scattering intensity between the determined dispersion using the H_{Jex} model and the resolution corrected H_{Jex} model in Table I. (d) Scattering intensity determined using the resolution corrected H_{Jex} model in Table I. Results in (a), (c), and (d) have been smoothed by a Gaussian smoothing algorithm.

Figure 5 shows a series of constant wave-vector scans through the CNCS and SEQUOIA measurements. The solid and dotted lines in this figure are parameterizations of the scattering intensity using Gaussian line-shapes with sloping backgrounds fit to the respective data. One

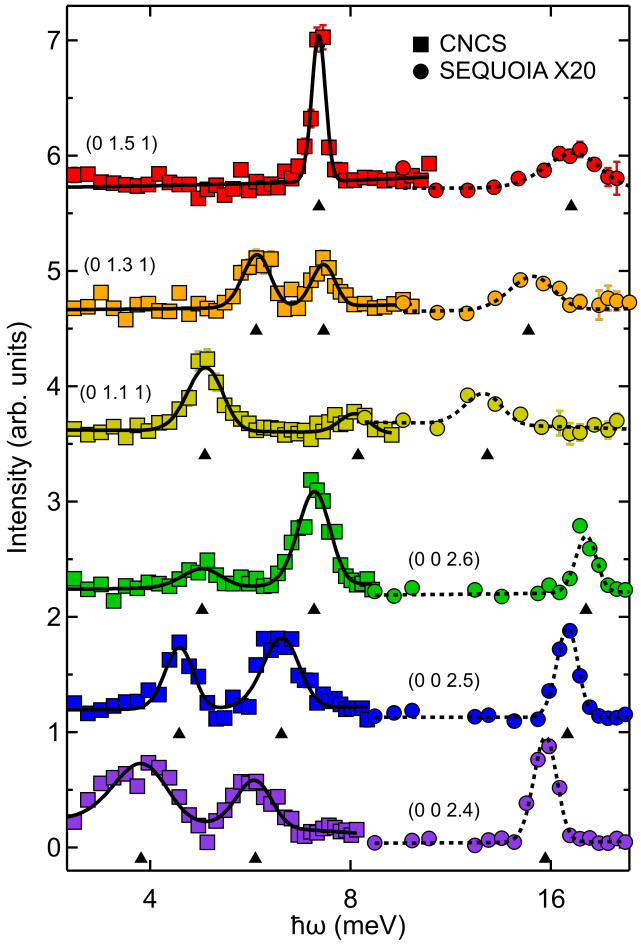

FIG. 5: Inelastic neutron scattering measurements of $Mn_3Si_2Te_6$ plotted as constant wave-vector scans from the $T = 5$ K CNCS (■) and SEQUOIA (•) measurements. Data have been offset along the vertical axis for presentation. The SEQUOIA measurements have been scaled by a factor of 20 to place them on the same intensity scale as the CNCS measurements. Solid (CNCS data) and dotted (SEQUOIA data) lines are comparisons of the measurement to either a single Gaussian with a sloping background or two Gaussians with a sloping background as described in the text. Data correspond to the wave-vectors indicated in the figure. Data were integrated over the symmeterized slices shown in Fig. 3(a) and (d) without any smoothing over a range of ±0.05 rlu. Black triangles are the fitted Gaussian peak locations for the respective modes they are beneath.

can observe the presence of multiple modes and the dispersion in these modes as a function of wave-vector transfer. This procedure was extended to include 32 wave-vectors throughout the measured volume of reciprocal space. These points were along the $(0K1)$, $(00L)$, $(H00)$, $(H01)$, $(H02)$, $(H03)$, and $(H0H)$ wave-vectors. Figures 3(e)-(h) and 4(b) show the fitted peak locations and the determined mode energy from many of these fitted wave-vectors (solid symbols).

Considering the classical magnetic moment on Mn^{2+}

to be $S = 5/2$, and the spin ordered magnetic structure, we use linear spin-wave (LSW) theory to calculate the magnetic excitations in order to determine the nature of the magnetic Hamiltonian. Prior first-principles calculations found that three competing anti-ferromagnetic Heisenberg exchange interactions, J_1, J_2, and J_3 as illustrated in Fig. 1, are able to account for the long range ordered structure and the apparent suppression in the ordering temperature[19]. Note that a small spin-orbit coupling was previously considered to account for exchange anisotropies. Using the determined dispersion shown in Fig. 3(e)-(h), we performed a refinement of the spin-wave dispersion using the spinW software[26].

We first attempt to model the data using the Heisenberg Hamiltonian with the potential for only on-site anisotropies (i.e. single ion):

$$H_{XY} = J_1 \sum_{\langle i,j \rangle} \mathbf{S}_i \mathbf{S}_j + J_2 \sum_{\langle i,j \rangle} \mathbf{S}_i \mathbf{S}_j + J_3 \sum_{\langle i,j \rangle} \mathbf{S}_i \mathbf{S}_j + D_H \sum_h S_h^z S_{\bar{h}}^z + D_T \sum_t S_t^z S_t^z, \quad (1)$$

where the summation for the Heisenberg exchange is restricted to the relevant nearest neighbors, D_H and D_T corresponding to the on-site anisotropy in the honeycomb and triangular lattice layers respectively, while the sums for the D terms are only for moments in the respective layers. A refinement of the pure Heisenberg model yields the terms $J_1 = 1.398(3)$, $J_2 = 0.230(10)$, $J_3 = 0.718(10)$ meV. The pure Heisenberg model is not able to account for the gap in energies between mode branches.[25] Including on site anisotropy, yields similar values for the exchange terms $J_1 = 1.400(6)$, $J_2 = 0.261(8)$, $J_3 = 0.776(9)$, and small values of single ion anisotropy, $D_H = 0.08(2)$ and $D_T = 0.08(2)$ meV. This model also is not able to account for the gap between the lower and upper band of magnetic excitations between approximately 10 and 12 meV.[25] We quantify the resulting value by comparing the measured scattering intensity shown in Fig. 3(a)-(d) to the resolution convolved scattering intensity for these directions using a single constant background and a multiplicative scale factor for the scattering intensity for each of the wave-vector directions shown. The chi-square value for this comparison of the dispersion points is $\chi^2 = 2.55$ and $\chi^2 = 2.46$ respectively as shown in Table I.[27]

A Hamiltonian without on-site anisotropy, but which allows for anisotropic exchange interactions to account for the spin-orbit coupling previously described was also considered:

$$\begin{aligned} H_{Jex} = \; & J_1 \sum_{\langle i,j \rangle} [S_i^x S_j^x + S_i^y S_j^y + \Delta_1 S_i^z S_j^z] + \\ & J_2 \sum_{\langle i,j \rangle} [S_i^x S_j^x + S_i^y S_j^y + \Delta_2 S_i^z S_j^z] + \\ & J_3 \sum_{\langle i,j \rangle} [S_i^x S_j^x + S_i^y S_j^y + \Delta_3 S_i^z S_j^z] \end{aligned} \quad (2)$$

where the summation is restricted to the relevant nearest neighbours. Allowing the values of Δ_1, Δ_2, and Δ_3 to independently vary, improves substantially the comparison with the data and yields an improved refined dispersion with $J_1 = 1.508(4)$ meV, $J_2 = 0.457(4)$ meV, $J_3 = 0.912(8)$ meV, $\Delta_1 = 1.140(9)$, $\Delta_2 = 0.0138(7)$, and $\Delta_3 = 0.621(9)$ with $\chi^2 = 1.74$. Deviations from unitary values of Δ quantify the extent of spin-orbit interactions. The refined Δ terms indicate that the Mn1 sites are experiencing a greater influence of the spin-orbit interaction compared to the Mn2 sites. The dispersion is shown in Fig. 3(e)-(h) and 4. Importantly, this improved refinement reproduces the gap between the high and low energy bands and therefore indicates that an apparent easy plane anisotropy is responsible for this feature in the spectrum. This anisotropy is a manifestation of the weak spin-orbit coupling in the compound.[19]

A. Image Analysis of Dispersion

The refinement process just described, however, does not account for instrumental resolution effects which will often serve to sharpen or broaden dispersion relative to one another, or shift dispersions depending upon focusing effects across the spectrum. Here we describe an extension of an image analysis technique for the refinement of spin-wave dispersions that includes resolution effects. The energy resolution of the SEQUOIA measurement across the energy transfer range of 12 to 22 meV energy transfer varies between 3.4 to 2.8 meV FWHM, corresponding to a value of $\delta\hbar\omega/E_i = 5\%$.[28] The energy resolution of the CNCS measurement between 0 and 10 meV energy transfer varies between 0.7 to 0.4 meV FWHM, corresponding to a value of $\delta\hbar\omega/E_i = 3 - 6\%$ for this range. We anticipate that resolution effects will be more significant in the determination of the dispersion from the SEQUOIA measurement.

From the first refined values of the Hamiltonian presented in Tab. I for Eq. 2, we can calculate the resolution convolved scattering intensities, where the resolution function is calculated from MCViNE[29,30] simulations using the dgsres package[31]. From this initial simulation, one can extract a series of constant wave-vector scans and refine peak locations of this calculated data using a Gaussian line-shape, following the same procedure that was performed on the real experimental data. These extracted peak locations of the resolution-convolved model, $E_{\mathrm{sim};0}(q)$, can be compared with the values of the dispersion determined at the respective wave-vectors directly from the experimental data, $E_{\mathrm{exp};0}(q)$. Their differences $\Delta E(q) = E_{\mathrm{exp};0}(q) - E_{\mathrm{sim};0}(q)$ can be used to correct the dispersion directly obtained from experimental data. However, such an approach is prone to unstable results for $\Delta E(q)$. Instead, a procedure inspired by the image disparity-map calculation technique was performed. This procedure solves the $\Delta E(q)$ curve by imposing a smoothness regularization.[32] The disper-

Hamiltonian	J_1 (meV)	J_2 (meV)	J_3 (meV)	D_H	D_T	Δ_1	Δ_2	Δ_3	$\chi^2_{disp.}$	χ^2
Heisenberg	1.398(3)	0.230(10)	0.718(10)	—	—	—	—	—	2.55	3.12
H_{XY}	1.400(6)	0.261(8)	0.776(9)	0.08(2)	0.08(2)	—	—	—	2.46	3.82
H_{Jex}	1.508(4)	0.457(4)	0.912(8)	—	—	1.140(9)	0.0138(7)	0.621(9)	1.74	3.31
$H^{\text{res.}}_{Jex}$	1.509(9)	0.449(3)	0.859(4)	—	—	1.171(6)	0.0271(8)	0.625(3)	—	2.24

TABLE I: Refined values of the exchange constants for $Mn_3Si_2Te_6$, for each model implemented in our refinement. The parameters determined from the resolution corrected dispersion are shown for the Hamiltonian $H^{\text{res.}}_{Jex}$. The values of $\chi^2_{disp.}$ were determined from the spinW software fitting the dispersion data. The values for χ^2 were determined through a comparison of the measured and calculated scattering intensity for the data shown in Fig. 3(a)-(d) as described in the text.[27]

sion from the resolution-convolved data in the SEQUOIA measurement are systematically too high in energy transfer. This is a consequence of the three-dimensional dispersion surface and the steep dispersion in the vicinity of the anti-ferromagnetic zone centers convolved with the instrumental resolution of SEQUOIA operating in the high flux configuration. We determine the shifts in energy transfer, $\Delta E(q)$, for a series of wave-vectors along the $[00L]$, $[H03]$, $[H0H]$, $[1K0]$, and $[H01]$ directions for both the SEQUOIA and CNCS measurements. Regions of wave-vector transfer with good signal to noise ratios were chosen for this portion of the analysis to allow ultimately for direct comparison of the resolution convolved scattering intensity with the measured data. To first approximation, we correct for the resolution effects by applying the shifts $\Delta E(q)$ to the model dispersion directly obtained from experimental slices:

$$E_{\text{exp;}\,1}(q) = E_{\text{model;}\,0}(q) + \Delta E(q) \qquad (3)$$

These shifted values of energy transfer are shown with the values originally determined via a Gaussian lineshape approximation in Figs. 3(e),(g), and (h), 4(b) as heavy solid lines. The spin-wave dispersion of the anisotropic Heisenberg exchange model, Eq. 2, can then be refined using the resolution function shifted peak locations, $E_{\text{exp;}\,1}(q)$. This results in the exchange constants and anisotropy terms shown in Tab. I for the $H^{\text{res.}}_{Jex}$ model. Values of reduced chi square based upon a comparison of the measured and calculated scattering intensity for a subset of wave-vector transfers along the $[00L]$, $[H03]$, $[H0H]$ and $[1K0]$ directions can be calculated for the models examined and the resolution corrected model. Originally, using the uncorrected values of the dispersion, the reduced chi square value was 3.31, this value decreased to 2.24 once the resolution correction was applied.[27]

The resulting refined dispersion curves for the resolution corrected model,$H^{\text{res.}}_{Jex}$ are shown in Figs. 3(e)-(h) and 4(b). The refined and best exchange parameters are $J_1 = 1.509(9)$ meV, $J_2 = 0.449(3)$ meV, $J_3 = 0.859(4)$ meV, $\Delta_1 = 1.171(6)$, $\Delta_2 = 0.0271(8)$, and $\Delta_3 = 0.625(3)$. Figure 4(c) shows the change in scattering intensity of the calculated resolution convolved scattering intensity between the original and the resolution convolved H_{Jex} models. There are significant changes in the vicinity of the dispersive modes. One can also see the effects of the focused and defocused resolution condition on the SEQUOIA portion of the measurement. As visible, there is a greater shift in the calculated intensity in the vicinity of the local minima and maxima at the dispersion zone boundaries, while near flat regions of the dispersion are not significantly affected by the resolution effects. Figs. 3(i)-(l) and 4(d) are the calculated resolution convolved scattering intensity for the anisotropic exchange model determined from the resolution corrected dispersion, $H^{\text{res.}}_{Jex}$. The comparison with the measured data is very good over wide ranges of energy and wave-vector transfer. We note that there are regions with lingering disparity between the measurement and the model. This includes data in the vicinity of 7 meV energy transfer and half integer wave-vectors as shown in Fig. 4(a) and Fig. 3(b-d). The SEQUOIA measurements indicate that this region likely includes an optic or acoustic phonon that is contributing increasing scattering intensity at larger wave-vector transfer, see for example $[\frac{1}{2}03]$ and $[\frac{3}{2}03]$ in Fig. 3(b).

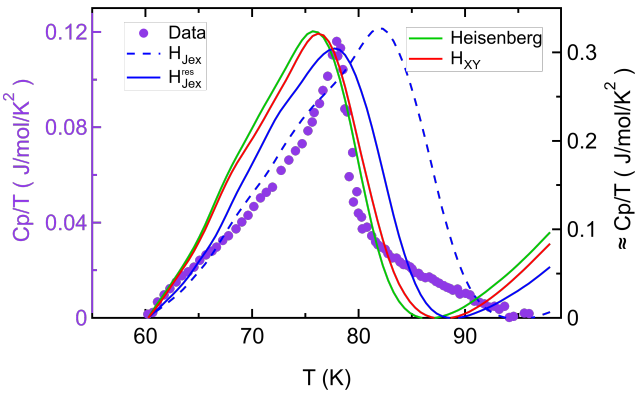

FIG. 6: Temperature normalized heat capacity as a function of temperature for $Mn_3Si_2Te_6$. Data are shown as purple circles plotted on the left axis. Lines (right axis) are the Monte Carlo calculation performed using Eq. 4 for the models tabulated in Table I.

An independent validation of the determined Hamiltonian can be made by calculating thermodynamic quantities like heat capacity, which is a measurement of the

energy fluctuations in the system. The heat capacity comparison shown in Fig. 6, is calculated via a standard Metropolis sampling algorithm by averaging over 96 independent sets of simulations on a $8 \times 8 \times 4$ super-cell (1536 spins). The system has been slowly annealed from T=300 K, down to T=50 K, with 100 intermediate temperatures. At each temperature, the heat capacity is calculated by the total energy fluctuations (see Eq. 4) over 10^6 Monte Carlo updates to ensure convergence, followed by a thermalisation process with automatic termination. Thus:

$$C_v = R\frac{\langle E^2\rangle - \langle E\rangle^2}{T^2} \tag{4}$$

where R is the gas constant and $\langle E\rangle$ represent the energy fluctuation of a spin configuration at fixed temperature T. We perform this calculation for the Heisenberg, H_{XY}, H_{Jex}, and $H_{Jex}^{\text{res.}}$ models in Table I. Finally, our Monte Carlo predicts the correct spin orientation in the ordered phase at $T = 0$ K, consistent with Ref.[19] further validating the proposed Hamiltonian. The peak location in the calculated heat capacity is found to agree very well with the $H_{Jex}^{\text{res.}}$ model's refined parametres.

IV. CONCLUSIONS

The magnetic Hamiltonian of $Mn_3Si_2Te_6$ was investigated by measuring its spin wave dispersion at T=5 K. The analysis of the data collected at SEQUOIA and CNCS, confirmed the predictions on the spin orientation of this compound below its transition temperature with ferrimagnetic coupled spins. A neutron event based azimuthal background subtraction was developed to improve the range of wave-vector and energy transfer over which the dispersion could be quantified. An efficient method of refining the terms in the Hamiltonian while accounting for resolution effects was also demonstrated. This allows one to refine the nature of the excitation spectrum including resolution effects without relying on the computationally intensive full numerical convolution of the resolution function with the model at every step of the model's refinement in a fitting algorithm.

The ratios of the determined exchange values, J_1, J_2, and J_3 shown in Tab I agree reasonably well with the predictions in Ref.[19]. The underlying hexagonal layers in the crystal structure, the near crossing bands in the dispersion, and the presence of spin-orbit coupling suggests topological implications and the possibility of Dirac points in the dispersion. These points would occur where the spin-wave bands approach one another at similar locations in reciprocal space to such points in other compounds.[33–35] However, the Berry curvature for these points in $Mn_3Si_2Te_6$ all have a value of zero indicating that the near crossing points are not Dirac or Weyl points.[36,37] Nonetheless, our work establishes $Mn_3Si_2Te_6$ as a good example of a compound with a dispersion influenced by spin-orbit interactions and significant magnetic exchange orthogonal to a layered structure. It was found recently that one mechanism to tune the magnetization of $Mn_3Si_2Te_6$ is to use proton irradiation.[38] Our characterization of the energy scales present for the exchange interactions in $Mn_3Si_2Te_6$ may provide further understanding to the mechanism at play in the proton irradiation studies.

V. ACKNOWLEDGMENTS

This work was supported by the US Department of Energy, Office of Science, Basic Energy Sciences, Materials Sciences and Engineering Division. Work at ORNL's Spallation Neutron Source was supported by the Scientific User Facilities Division, Office of Basic Energy Sciences, US Department of Energy (DOE). We acknowledge useful discussions with C. Batista that helped us in the preparation of this manuscript. We acknowledge J. Leiner and A. Savici for useful discussions regarding background subtraction. We acknowledge Hao Zhang for useful discussions regarding Berry curvature calculations.

† Electronic address: stonemb@ornl.gov

[1] S. Tian, J.-F. Zhang, C. Li, T. Ying, S. Li, X. Zhang, K. Liu, and H. Lei, Journal of the American Chemical Society **141**, 5326 (2019), pMID: 30856325, https://doi.org/10.1021/jacs.8b13584 .
[2] C. Gong, L. Li, Z. Li, H. Ji, A. Stern, Y. Xia, T. Cao, W. Bao, C. Want, Y. Wang, Z. Qiu, R. Cava, S. Louie, J. Xia, and X. Zhang, Nature **546**, 265 (2017).
[3] B. Huang, G. Clark, E. Navarro-Moratalla, D. Klein, R. Cheng, K. Seyler, D. Zhong, E. Schmidgall, M. McGuire, D. Cobden, W. Yao, D. Xiao, P. Jarillo-Herrero, and X. Xu, Nature **546**, 270 (2017).
[4] X. Shi, I. K. Dimitrov, T. Ozaki, G. Gu, and Q. Li, Phys. Rev. B **96**, 184519 (2017).
[5] P. Dai, Rev. Mod. Phys. **87**, 855 (2015).
[6] N. M. Hassan, K. Thirunavukkuarasu, Z. Lu, D. Smirnov, E. I. Zhilyaeva, S. Torunova, R. N. Lyubovskaya, and N. Drichko, Phys. Rev. B **104**, 245120 (2021).
[7] C. Wang, M.-q. Tan, C.-m. Feng, Z.-f. Ma, S. Jiang, Z.-a. Xu, G.-h. Cao, K. Matsubayashi, and Y. Uwatoko, Journal of the American Chemical Society **132**, 7069 (2010), https://doi.org/10.1021/ja1001295 .
[8] B. C. Sales, J. Yan, W. R. Meier, A. D. Christianson, S. Okamoto, and M. A. McGuire, Phys. Rev. Materials **3**, 114203 (2019).
[9] S.-H. Do, K. Kaneko, R. Kajimoto, K. Kamazawa, M. B. Stone, J. Y. Y. Lin, S. Itoh, T. Masuda, G. D. Samolyuk, E. Dagotto, W. R. Meier, B. C. Sales, H. Miao, and A. D. Christianson, Phys. Rev. B **105**, L180403 (2022).
[10] Y. Liu, N. Weiss, X. Duan, H.-C. Cheng, Y. Huang, and

X. Duan, Nature Reviews Materials **1**, 16042 (2016).
[11] D. Zhong, K. L. Seyler, X. Linpeng, R. Cheng, N. Sivadas, B. Huang, E. Schmidgall, T. Taniguchi, K. Watanabe, M. A. McGuire, W. Yao, D. Xiao, K.-M. C. Fu, and X. Xu, Science Advances **3** (2017), 10.1126/sciadv.1603113, https://advances.sciencemag.org/content/3/5/e1603113.full.pdf .
[12] K. L. Seyler, D. Zhong, B. Huang, X. Linpeng, N. P. Wilson, T. Taniguchi, K. Watanabe, W. Yao, D. Xiao, M. A. McGuire, K.-M. C. Fu, and X. Xu, Nano Letters **18**, 3823 (2018), pMID: 29756784, https://doi.org/10.1021/acs.nanolett.8b01105 .
[13] D. Lançon, H. C. Walker, E. Ressouche, B. Ouladdiaf, K. C. Rule, G. J. McIntyre, T. J. Hicks, H. M. Rønnow, and A. R. Wildes, Phys. Rev. B **94**, 214407 (2016).
[14] T. J. Williams, A. A. Aczel, M. D. Lumsden, S. E. Nagler, M. B. Stone, J.-Q. Yan, and D. Mandrus, Phys. Rev. B **92**, 144404 (2015).
[15] S. Calder, A. V. Haglund, A. I. Kolesnikov, and D. Mandrus, Phys. Rev. B **103**, 024414 (2021).
[16] L. Chen, J.-H. Chung, T. Chen, C. Duan, A. Schneidewind, I. Radelytskyi, D. J. Voneshen, R. A. Ewings, M. B. Stone, A. I. Kolesnikov, B. Winn, S. Chi, R. A. Mole, D. H. Yu, B. Gao, and P. Dai, Phys. Rev. B **101**, 134418 (2020).
[17] H. Vincent, D. Leroux, D. Bijaoui, R. Rimet, and C. Schlenker, Journal of Solid State Chemistry **63**, 349 (1986).
[18] R. Rimet, C. Schlenker, and H. Vincent, Journal of Magnetism and Magnetic Materials **25**, 7 (1981).
[19] A. F. May, Y. Liu, S. Calder, D. S. Parker, T. Pandey, E. Cakmak, H. Cao, J. Yan, and M. A. McGuire, Phys. Rev. B **95**, 174440 (2017).
[20] A. F. May, H. Cao, and S. Calder, Journal of Magnetism and Magnetic Materials **511**, 166936 (2020).
[21] G. E. Granroth, A. I. Kolesnikov, T. E. Sherline, J. P. Clancy, K. A. Ross, J. P. C. Ruff, B. D. Gaulin, and S. E. Nagler, Journal of Physics: Conference Series **251**, 012058 (2010).
[22] G. Ehlers, A. A. Podlesnyak, J. L. Niedziela, E. B. Iverson, and P. E. Sokol, Review of Scientific Instruments **82**, 085108 (2011), https://doi.org/10.1063/1.3626935 .
[23] O. Arnold, J. Bilheux, J. Borreguero, A. Buts, S. Campbell, L. Chapon, M. Doucet, N. Draper, R. Ferraz Leal, M. Gigg, V. Lynch, A. Markvardsen, D. Mikkelson, R. Mikkelson, R. Miller, K. Palmen, P. Parker, G. Passos, T. Perring, P. Peterson, S. Ren, M. Reuter, A. Savici, J. Taylor, R. Taylor, R. Tolchenov, W. Zhou, and J. Zikovsky, Nuclear Instruments and Methods in Physics Research Section A: Accelerators, Spectrometers, Detectors and Associated Equipment **764**, 156 (2014).
[24] J. Leiner, H. Jeschke, R. Valent, S. Zhang, A. Savici, J. Lin, M. Stone, M. Lumsden, J. Hong, O. Delaire, W. Bao, and C. Broholm, Physical Review X **9** (2019), 10.1103/PhysRevX.9.011035.
[25] See Supplemental Material at [URL will be inserted by publisher] for further details.
[26] S. Toth and B. Lake, Journal of Physics: Condensed Matter **27**, 166002 (2015).
[27] We calculate χ^2 as $\chi^2 = \Sigma_i \frac{(O_i - E_i)^2}{E_i}$, where O_i is the observed intensity and E_i is the calculated intensity.
[28] Abernathy, D.L., Niedziela, J.L., and Stone, M.B., EPJ Web of Conferences **83**, 03001 (2015).
[29] J. Y. Lin, H. L. Smith, G. E. Granroth, D. L. Abernathy, M. D. Lumsden, B. Winn, A. A. Aczel, M. Aivazis, and B. Fultz, Nuclear Instruments and Methods in Physics Research Section A: Accelerators, Spectrometers, Detectors and Associated Equipment **810**, 86 (2016).
[30] J. Y. Lin, F. Islam, G. Sala, I. Lumsden, H. Smith, M. Doucet, M. B. Stone, D. L. Abernathy, G. Ehlers, J. F. Ankner, *et al.*, Journal of Physics Communications **3**, 085005 (2019).
[31] "dgsres: Neutron direct geometry spectrometer resolution calculators," `https://doi.org/10.5281/zenodo.5137820` (2021).
[32] J. Y. Y. Lin, G. Sala, and M. B. Stone, Review of Scientific Instruments **93**, 025101 (2022), https://doi.org/10.1063/5.0079031 .
[33] L. Chen, J.-H. Chung, M. B. Stone, A. I. Kolesnikov, B. Winn, V. O. Garlea, D. L. Abernathy, B. Gao, M. Augustin, E. J. G. Santos, and P. Dai, Phys. Rev. X **11**, 031047 (2021).
[34] B. Yuan, I. Khait, G.-J. Shu, F. C. Chou, M. B. Stone, J. P. Clancy, A. Paramekanti, and Y.-J. Kim, Phys. Rev. X **10**, 011062 (2020).
[35] A. Sapkota, L. Classen, M. B. Stone, A. T. Savici, V. O. Garlea, A. Wang, J. M. Tranquada, C. Petrovic, and I. A. Zaliznyak, Phys. Rev. B **101**, 041111 (2020).
[36] S.-S. Zhang, H. Ishizuka, H. Zhang, G. B. Halász, and C. D. Batista, Phys. Rev. B **101**, 024420 (2020).
[37] R. Matsumoto, R. Shindou, and S. Murakami, Phys. Rev. B **89**, 054420 (2014).
[38] L. M. Martinez, C. L. Saiz, A. Cosio, R. Omos, H. Iturriaga, L. Shao, and S. R. Singamaneni, MRS Advances **4**, 2177 (2019).